BloEx - Journal
Britain International of
EXACT Sciences Journal
Publish: | January - May - September |
E-ISSN: 2686-1208
P-ISSN: 2686-1216
http://biarjournal.com/index.php/bioex

Study, Design and Development of an Electric Crucible Furnace for Laboratory Use from Local Malagasy Raw Materials

Rafanomezantsoa Elia Metosaela[1], Robijaona Rahelivololoniaina Baholy[1,2]
[1]Higher Polytechnic School of Antananarivo, University of Antananarivo, Antananarivo, Madagascar
[2]Graduate School of Industrial, Agricultural, and Food Process and Systems Engineering, University of Antananarivo, Antananarivo, Madagascar
Email: metosaelaerafa26@gmail.com

Abstract:

This study addresses the critical challenge of high-temperature laboratory equipment acquisition in developing regions by validating the technical and economic feasibility of fabricating an electric crucible furnace utilizing regional Malagasy resources. The physicochemical and mineralogical traits of four local raw materials – refractory clay, Vontovorona kaolin, Mahela graphite, and rice husk ash – were systematically characterized to establish an unprecedented regional materials database. Six distinct ternary composite formulations were developed and fired under localized protocols to produce high-temperature insulating bricks. Microstructural testing revealed that all configurations achieved excellent thermal stability, marked by residual mineral ash yields exceeding 95.00% and an optimized open porosity framework spanning 38.13% to 45.50%. Formulation E6, composed of an equimass clay-to-kaolin ratio, demonstrated the highest structural consolidation, exhibiting relative increases of 72.6% in splitting tensile strength and 90.8% in uniaxial compressive strength (reaching 1.845 MPa) compared to the baseline mixture. Practical operational validation was successfully achieved through aluminum scrap recycling trials, during which the integrated Proportional-Integral-Derivative (PID) control loop, solid-state relays, and Type-S thermocouple maintained a stable process temperature of 800°C. Economically, the total production cost of 653,410 MGA represents a tenfold reduction compared to imported commercial counterparts. By bridging traditional low-cost artisanal fabrication methods with high-precision electronic thermal regulation, this research introduces a highly transferable intermediate technology model. This prototype successfully fosters circular economy pathways via localized non-ferrous metallurgy while providing a reproducible framework for equipping academic and research laboratories across the sub-region at minimal cost.

Keywords:
electric furnace; refractory materials; kaolin; local valorization; crucible

I. Introduction

The optimization of high-performance thermal equipment remains a critical imperative within contemporary scientific research and pedagogical training infrastructure. In developing economies, access to certified, laboratory-grade furnaces is severely restricted by prohibitive acquisition costs and complex international logistical constraints. Madagascar possesses extensive, yet largely underutilized, mineral and agricultural sub-products—including refractory clays, kaolin, graphite, and rice husk ash—which offer significant potential for the local synthesis of advanced scientific apparatus. Although conventional electric crucible furnaces are widely deployed in metallurgical and foundry applications, their adaptation into versatile, bench-scale didactic units requires the rigorous integration of stringent safety protocols, precise thermal regulation, and structural compactness (Mullinger & Jenkins, 2014).

Currently, Malagasy academic and industrial laboratories specializing in chemical engineering and extractive metallurgy experience a critical deficit in reliable thermal infrastructure, which severely hinders the execution of reproducible high-temperature protocols. Commercially available imported furnaces on the domestic market command prohibitive prices ranging from 5,000,000 to 10,000,000 MGA, effectively rendering essential thermochemical processes inaccessible for institutional research and student training. Furthermore, the synthetic refractory liners utilized in these commercial systems are systematically imported, representing a missed opportunity for the strategic valorization of local geological resources. This systemic deficiency prompts a fundamental techno-economic research question: can a functional, high-temperature electric crucible furnace be engineered exclusively from Malagasy raw materials to meet international scientific standards while remaining economically viable?

To address this challenge, the primary objective of this investigation is to design, fabricate, and experimentally validate a prototype electric crucible furnace tailored for chemical engineering and metallurgical laboratories, relying strictly on locally sourced materials from Madagascar. The specific operational objectives comprise : (i) the comprehensive physico-chemical and mineralogical characterization of local refractory raw materials; (ii) the formulation and optimization of composite refractory mixtures dedicated to the synthesis of the heating chamber linings; (iii) the thermal and structural dimensioning of the overall furnace architecture ; and (iv) the empirical validation of thermal performance through controlled aluminum melting assays.

The underlying research hypothesis posits that a synergistic formulation of local argillaceous matrices—specifically refractory clay, Vontovorona kaolin, Mahela graphite, and rice husk ash—can yield composite refractory bricks exhibiting the precise thermomechanical properties required to sustain a continuous operating temperature of 1,000 °C, while reducing manufacturing costs to a fraction of commercial alternatives.

II. Research Method

2.1 Refractory raw materials

The selection of the primary constituents was governed by their domestic abundance within the Malagasy territory and their specific inherent thermomechanical behaviors. The baseline refractory clay was recovered from post-industrial fragments of locally fired earthenware pottery obtained from traditional artisanal networks. This argillaceous material exhibits high concentrations of Al_2O_3 and SiO_2, which are critical for establishing a stable mullite matrix during high-temperature sintering (Tychanicz-Kwiecien et *al.*, 2019). Kaolin was extracted from the geological deposits of the Vontovorona quarry; it is characterized by an elevated kaolinite content, low plasticity index, and a thermal deformation threshold exceeding 1,700 °C following appropriate thermal activation (Sadik et *al.*, 2014).

Agricultural waste valorization was achieved by integrating rice husk ash (RHA) sourced from regional brick-manufacturing facilities, serving as an abundant vector of highly reactive amorphous silica (Zareei et *al.*, 2019). Natural graphite flakes were acquired from the Mahela mining concession located within the Brickaville district; this material exhibits a high elemental carbon purity of 95.80% and a loose bulk density of 0.55 g/cm³. Structural binding and geopolymerization mechanisms were promoted via commercial sodium silicate ($Na_2O{\cdot}SiO_2$)

supplied by SPCI (Société de Produits Chimiques Industriels or Industrial Chemicals Company), characterized by a chemical composition of 12.56% Na_2O and 29.90% SiO_2. Commercial Portland cement (Grade CEM I) was selected as an auxiliary hydraulic binder due to its chemical compatibility with aluminosilicate networks (**Pera & Ambroise, 2004**). Naturally occurring spring water was utilized as the liquid medium for all formulation, hydration, and mixing procedures.

2.2 Electrical and electronic components

Thermal energy generation within the heating chamber relies on high-specification Kanthal A1 resistive elements composed of a ferritic iron-chromium-aluminum alloy (FeCrAl: 70.7 wt.% Fe, 23.5 wt.% Cr, 5.8 wt.% Al) displaying a nominal electrical resistivity of 1.45 $\Omega \cdot mm^2/m$ and a maximum continuous operating limit of 1,400 °C (Rawat & Shah, 1980).

The automated thermal regulation system consists of a digital REX C400 FK02-M*AN proportional-integral-derivative (PID) controller interfaced with a 40DA solid-state relay (SSR). Precision temperature feedback within the high-temperature zone is achieved using a platinum-rhodium/platinum (Type S) WRP 100 thermocouple calibrated for an operating range of 0 °C to 1,300 °C (Chook & Tan, 2007). System electrical safety and overcurrent protection are ensured by an integrated network comprising a residual current circuit breaker, 15 A rated fuses, high-temperature silicone-sheathed copper conductors, and a centralized electrical distribution enclosure (Hosamani et *al.*, 2021).

2.3 Analytical equipment

The physical, mineralogical, and mechanical properties of the raw materials and consolidated specimens were quantified using an array of standardized laboratory instrumentation. Particle size classifications were conducted utilizing standardized AFNOR sieve columns. Sub-sieve particles were analyzed through sedimentation techniques using a high-precision hydrometer and controlled-temperature cylinders.

Plasticity thresholds were quantified using a standardized Casagrande liquid limit apparatus. True density measurements were executed using a calibrated glass pycnometer, while specific surface area measurements were derived from a Blaine air permeability apparatus equipped with a U-tube manometer. Thermal processing was performed using a laboratory drying oven and a programmable high-temperature muffle furnace. Mechanical characterization was achieved using a CONTROLS automated slurry mixer, a controlled-atmosphere hygrometric curing chamber, a Maurice PERRIER tensile testing machine (Model 41.5, calibration factor $K_1 = 0.0025$), and a calibrated CONTROLS hydraulic compressive press.

2.4 Furnace fabrication equipment

Structural molding of the prototype bricks was performed using custom-engineered timber molds measuring 20 × 9.5 × 9.5 cm. The structural outer casing of the furnace was constructed from repurposed cylindrical steel sheets derived from commercial metal drums. Thermal insulation barriers were established using expanded polystyrene (EPS) panels (thermal conductivity $\lambda = 0.033–0.038$ W/m·K) and industrial-grade glass wool blankets (thermal conductivity $\lambda = 0.030–0.040$ W/m·K, maximum continuous thermal threshold = 250 °C) (Papadopoulos, 2005). Spatial engineering, structural optimization, and electrical wiring diagrams were developed using AutoCAD and AutoCAD Mechanical Inventor computer-aided design software suites.

2.5 Experimental methods

a. Raw material preparation

The raw geological and agricultural materials were subjected to sequential mechanical and thermal conditioning. Initial particle size reduction was achieved via mechanical crushing followed by manual grinding in an agate mortar. The refined powders were subsequently transferred to a laboratory oven and dried at 103 ± 5 °C until a constant mass was reached, thereby removing unbonded moisture. Dry mechanical sieving was then executed to isolate distinct particle size fractions. Finally, calcination protocols were carried out within a muffle furnace to induce dehydroxylation of the kaolinite into highly reactive meta-kaolinite, and to optimize the amorphous status of the silica within the rice husk ash matrix.

b. Physico-chemical characterization

Analytical characterization protocols were executed across the specialized laboratories of the LNTPB (Laboratoire National des Travaux Publics et du Bâtiment or National Laboratory for Public Works and Building), OMNIS (Office des Mines Nationales et des Industries Stratégiques, or National Office for Mining and Strategic Industries.), and the Department of Chemical Engineering at ESPA (École Supérieure Polytechnique d'Antananarivo or Antananarivo Higher Polytechnic School). Particle size distributions for the coarser fractions of clay and kaolin were mapped using AFNOR (Association Française de Normalisation or French Standards Association) sieve columns, whereas the fine particulate fractions under 80 μm were characterized via sedimentation assays governed by Stokes' law. Free moisture content was determined gravimetrically through differential oven drying.

The rheological plasticity limits of the clay pastes were assessed via Atterberg limit protocols using the Casagrande apparatus, specifically defining the liquid limit (W_L) at the standard 25-blow threshold. Bulk density was computed through direct volumetric mass determinations within calibrated molds. The specific gravity of the fine fractions was monitored via pycnometry using distilled water displacement, and the specific surface area was derived through Blaine air permeability metrics operated at 20 ± 2 °C with a relative humidity maintained below 65%.

c. Refractory brick formulations

A experimental matrix consisting of six distinct formulations, designated E1 through E6, was established by systematically adjusting the mass ratios of refractory clay (ranging from 100 to 150 g) and kaolin (ranging from 50 to 100 g). Conversely, the mass proportions of the remaining constituents were held constant across all trials : 50 g of RHA, 25 g of Portland cement, 12 g of graphite, and 33.55 g of sodium silicate binder.

The fabrication sequence initiated with thorough dry blending of the powders, followed by the gradual introduction of water within an automated mixer to ensure spatial homogeneity. The homogenized pastes were transferred into 4 × 4 × 16 cm steel molds and compacted using a standardized drop-weight consolidation apparatus. The green compacts were subjected to a 24-hour preliminary curing phase in a cold chamber, followed by a 7-day open-air curing interval. Sintering of the consolidated bricks was executed in a digital muffle furnace at a peak temperature of 800 °C for a continuous period of 24 hours.

d. Mechanical testing protocols

Following a 7-day stabilization period inside a regulated hygrometric chamber, the sintered specimens were subjected to destructive mechanical testing. Tensile strength profiles were acquired using the Maurice PERRIER apparatus, where the maximum tensile stress was calculated using the operational formula:

σ_t = Scale reading x K_1
where K_1 = 0.0025. Subsequent to the tensile failure assays, the resulting half-specimens were immediately subjected to uniaxial compression tests on the CONTROLS hydraulic press. The nominal compressive strength (σ_c) was recorded as the arithmetic mean of the maximum compressive stresses sustained by the two complementary half-specimens.

e. Physical analyses

The open porosity (P, expressed in %) of the fired specimens was evaluated using the water saturation method and determined via the following relationship:

$$P = \frac{M_2 - M_1}{M_1} \times 100$$

where M_1 represents the initial dry mass and M_2 denotes the water-saturated mass. Loss on ignition, residual ash content (%C), and volatile matter content (%V) were verified gravimetrically by heating the specimens at 800 °C for one hour in a muffle furnace using the differential mass formulas:

$$\%C = \frac{M_f}{M_i} \times 100$$

$$\%V = \frac{M_i - M_f}{M_i} \times 100$$

where M_i and M_f correspond to the initial and final masses, respectively. Linear and volumetric drying-to-firing shrinkages—encompassing length ($\%R_L$), width ($\%R_l$), height ($\%R_H$), and total volume ($\%R_V$)—were precisely monitored by logging the multi-axis physical dimensions of the specimens before and after the sintering cycle using a calibrated digital vernier caliper.

f. Furnace design and assembly

The internal heating chamber of the prototype furnace was engineered with an octagonal geometric configuration, providing an effective internal volume of 23.206 liters, derived from a cross-sectional base area (Sb) of 814.25 cm^2 and a chamber height (H) of 28.5 cm. The primary thermal insulation envelope incorporates a dual-layer strategy consisting of a 3 cm thick industrial glass wool blanket coupled with a 2 cm thick external layer of expanded polystyrene (EPS).

The full-scale refractory blocks utilized for the final masonry of the core chamber were formulated with a specific bulk composition optimized for industrial performance (37.48% refractory clay, 30.00% kaolin, 9.37% RHA, 12.00% cement, 2.90% graphite, and 8.24% sodium silicate by weight, representing a cumulative batch mass of 53.35 kg). These full-scale blocks were fired using a traditional kiln configuration fueled by a mixture of rice husks and coal over a continuous 2-day thermal cycle.

The electrical schematic, control loops, and logic circuits were mapped using AutoCAD Electrical. Structural assembly proceeded sequentially by shaping the external cylindrical steel drum, installing the multi-layer insulation blankets, executing the internal masonry of the octagonal refractory core, and integrating the electronic PID control loop.

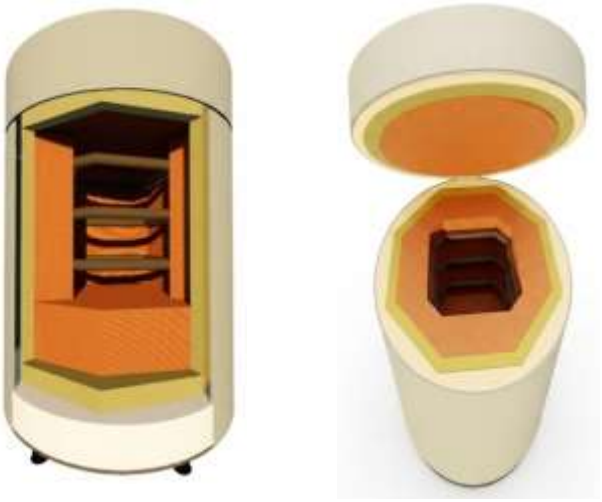

Figure 1: Three-dimensional view of the engineered electric crucible furnace prototype.

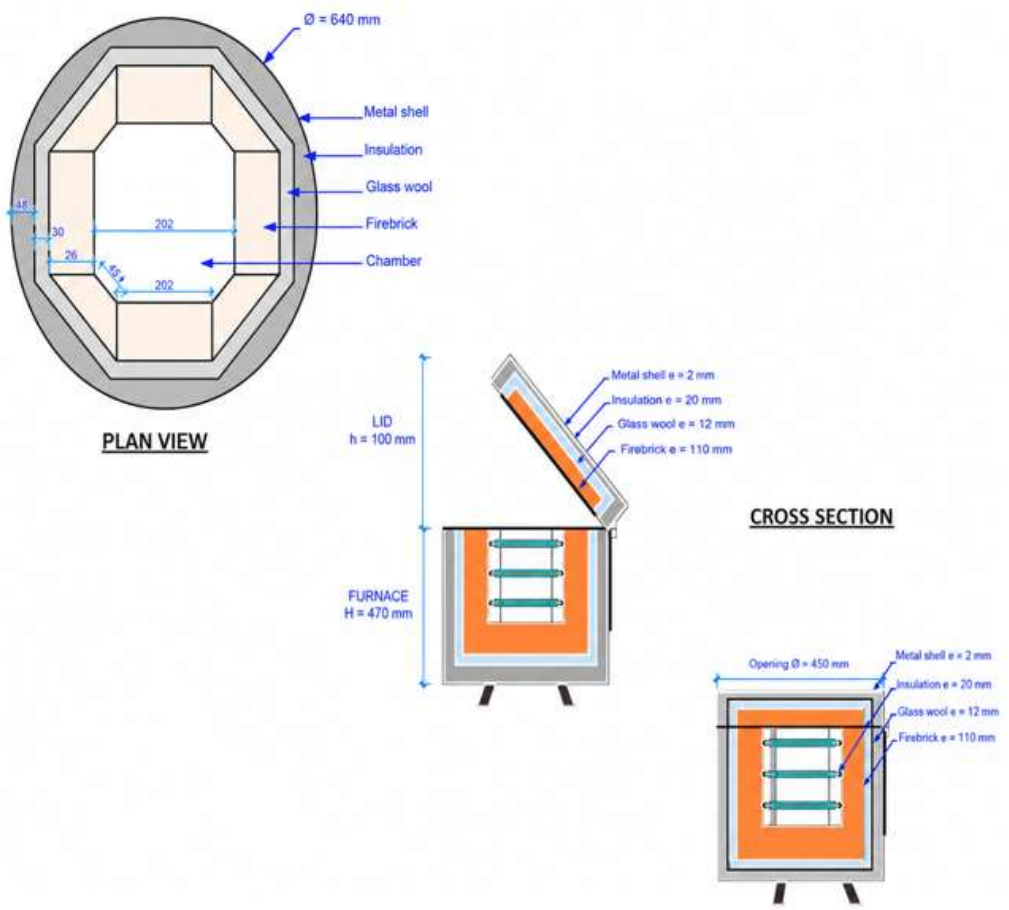

Figure 2: Complete multi-view technical drawing of the furnace assembly (comprising detailed front, profile, and plan views with comprehensive engineering dimensions.

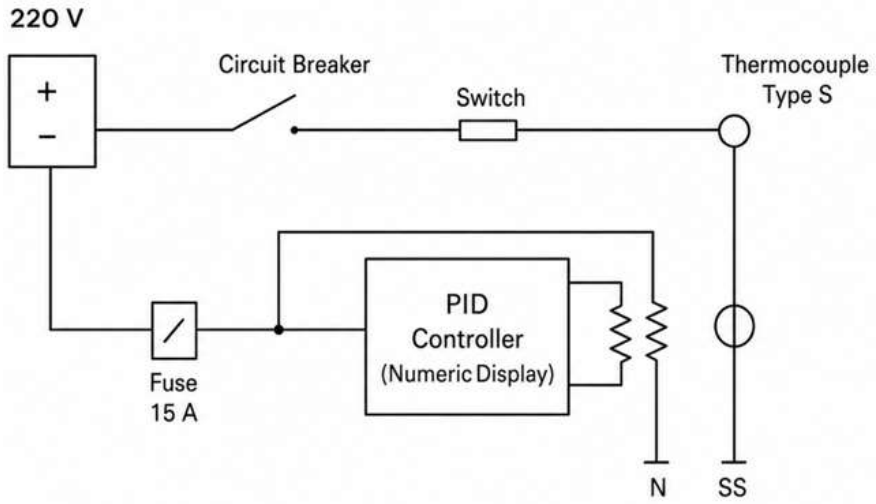

Figure 3: Integrated electrical schematic and PID control circuit configuration of the thermal unit

The structural representations confirm the geometric and thermal optimization of the prototype. The octagonal inner chamber (Figures 1 and **2**) minimizes dead zones to ensure uniform heat distribution, while the concentric insulation layers drastically restrict peripheral heat loss. Concurrently, the integrated control circuit (Figure 3) provides the automation necessary to secure precise, reproducible high-temperature cycles.

g. Thermal validation via aluminum melting assays

To empirically validate the structural integrity, thermal efficiency, and operational stability of the assembled furnace prototype under realistic laboratory conditions, melting trials were carried out using post-consumer aluminum beverage cans collected within the ESPA campus. The aluminum scrap was mechanically cleaned to remove organic contaminants, sectioned into high-density fragments, and charged into the crucible. The furnace was programmed to reach and maintain an operational temperature of approximately 800 °C. Once a uniform, fully liquid metallic bath was achieved, the molten aluminum was cast into standardized green sand molds and allowed to undergo solid-state cooling under ambient atmospheric conditions.

III. Result and Discussion

3.1 Moisture content of raw materials

Within the framework of valorizing local Malagasy raw materials for the synthesis of advanced refractory structures, the baseline moisture content constitutes a foundational parameter. This metric directly regulates the mixing water stoichiometry, mechanical densification during uniaxial pressing, and the magnitude of dimensional shrinkage occurring during subsequent thermal processing at 800 °C. The quantified hydro-values are compiled in Table 1.

Table 1. Moisture content profiles of the constituent refractory matrices

Parameter	Refractory clay	Kaolin	Rice Husk Ash (RHA)
Wet mass m_1 (g)	247.50	200.00	83.00
Dry mass m_2 (g)	243.47	191.79	80.42
Moisture content W (%)	1.66	4.28	3.21

Note. The gravimetric moisture content was derived using the standardized relationship:

$$W = \frac{m1 - m2}{m1} x\ 100$$

The Vontovorona kaolin displayed the highest initial moisture content (W = 4.28 %, corresponding to an absolute water mass of 8.21 g per 191.79 g of bone-dry matter). This elevated level dictates a proportional reduction in the exogenous mixing water volume to suppress excessive capillary tension during drying, thereby mitigating macro-crack propagation in the green compacts.

Conversely, the refractory clay exhibited a significantly lower moisture retention value of 1.66% (dry mass of 243.47 g), ensuring high structural stability during mechanical consolidation. When combined with the RHA fraction (W = 3.21 %), this ternary clay-kaolin-RHA matrix allows for precise control over the aggregate rheology, ultimately facilitating the formation of a micro-porous network that optimizes the thermal insulative performance of the core furnace assembly (Tychanicz-Kwiecien et *al.*, 2019).

a. Particle size analysis by sieving

The granulometric distribution of both the refractory clay and the kaolin plays a decisive role in governing the packing density of the granular skeleton and the localized surface reactivity during the 800 °C sintering stage. Analysis of the particulate fractions retained between the 80 µm and 2 mm thresholds allows for the optimization of the coarse-to-fine ratio, ensuring the attainment of target mechanical and thermal specifications.

Table 2. Granulometric classification of the local refractory clay matrix

AFNOR sieve aperture	Mean diameter Ø	Cumulative residue RC (g)	Cumulative residue RC (%)	Cumulative passing T (%)
2 mm	>2 mm	0	—	—
1 mm	1.5 mm	0	—	100
315 µm	657.5 µm	28.5	13.36	87
200 µm	257.5 µm	51.5	24.57	75
80 µm	140 µm	84.5	40.32	60

Note. Experimental conditions:
baseline moisture content W = 1.655 % ;
total wet mass M_{wet} = 213.00 g;
total dry mass M_{dry} = 209.53 g.

The cumulative residue retained at the 80 µm sieve reached 40.32% (84.5 g out of a total dry mass of 209.53 g), indicating that a dominant fraction of 59.68% of the constituent grains falls below the 140 µm threshold. This substantial fine fraction acts as a highly reactive filler, promoting the formation of an interconnected, high-density binding network during solid-state sintering, which enhances macro-structural cohesion.

The absolute absence of particulate fractions exceeding 2 mm confirms the exclusion of large, detrimental aggregate clusters that could introduce stress concentration zones. With a well-distributed cumulative residue of 13.36% at 315 µm, the clay displays a highly favorable continuous grading curve, maximizing green-state packing efficiency during the mechanical shaping of the heating chamber components.

Table 3. Granulometric classification of the vontovorona kaolin matrix

AFNOR sieve aperture	Mean diameter Ø	Cumulative residue RC (g)	Cumulative residue RC (%)	Cumulative passing T (%)
2 mm	>2 mm	5.5	2.86	97.0
1 mm	1.5 mm	25.0	13.04	87.0
315 µm	657.5 µm	55.0	28.68	71.0
200 µm	257.5 µm	81.0	42.25	58.0
80 µm	140 µm	97.5	50.85	49.0

Note. Experimental conditions:
baseline moisture content W = 4.280 %;
total wet mass M_{wet} = 200.00 g;
total dry mass M_{dry} = 191.79 g.

The Vontovorona kaolin recorded a cumulative residue of 50.85% at the 80 µm boundary (97.5 g retained from a dry mass of 191.79 g), which is 10.53 percentage points higher than the corresponding value for the refractory clay, thereby demonstrating a coarser granulometric profile. This textural divergence confirms the complementary nature of the two aluminosilicate sources : the kaolin fraction serves as a thermal stabilization framework by undergoing mullitization at elevated temperatures, whereas the finer clay matrix supplies the vital plastic properties necessary for molding operations (Sadik et *al.*, 2014).

Furthermore, the coarse fraction isolated between 315 µm and 2 mm represents 28.68% of the total kaolin volume, contrasting with the 13.36% monitored in the clay sample. This elevated coarse skeletal fraction within the kaolin serves to arrest volumetric contractions during the firing phase, ensuring excellent dimensional stability under high-temperature cycling.

b. Sedimentation analysis of the refractory clay matrix

Sedimentation kinetics based on Stokes' law allowed for the precise quantification of the sub-80 µm colloidal fraction inherent to the local refractory clay, which remains unresolved via standard dry sieving. Within the context of refining refractory formulations, tracking these sedimentation kinetics isolates the sub-micron phyllosilicate fractions that dictate the hydration capacity and inter-particle forces during mixing.

Table 4. Stokes'-law-based hydrometer sedimentation metrics for local refractory clay

Setting time t	Hydrometer reading R	Temperature T (°C)	Meniscus correction	Corrected reading R_1	Effective depth Ht (cm)	Particle diameter D (μm)	Passing fraction (%) grains <D
30 s	1.014	22.8	0.0033	0.0173	14.63	10	44.1
1 min	1.013	22.8	0.0033	0.0163	14.83	7.1	41.5
5 min	1.010	23.0	0.0033	0.0133	14.95	3.2	33.9
20 min	1.007	23.0	0.0033	0.0103	15.55	1.6	26.2
240 min	1.005	23.2	0.0031	0.0081	15.95	0.5	20.6
1,440 min	1.003	23.2	0.0032	0.0062	16.35	0.2	15.8

Note. Baseline physical constants:
specific gravity of solids $\square_s$ = 2.418 T/m^3;
acceleration due to gravity g = 981 cm/s^2;
density of water medium $\square_w$ = 0.998 g/cm^3.

At the 30-second measurement interval, 44.1% of the suspended clay mass exhibited an equivalent spherical diameter (D) below 10 μm, demonstrating a significant concentration of active clay minerals. Following a prolonged settling duration of 1,440 minutes, a stable fraction of 15.8% of ultra-fine particles remained in suspension at D < 0.2 μm, indicating the presence of highly active nanometric colloids typical of well-crystallized phyllosilicates.
The systematic increase in the effective settling depth (H_t moving from 14.63 cm to 16.35 cm) reflects a well-behaved, non-flocculated sedimentation profile. Concurrently, the corrected hydrometer values (R_1 descending from 0.0173 to 0.0062) match the specific sedimentation curves of kaolinite-illite mixed assemblages, which are highly efficient at generating high-cohesion ceramic bonds during thermal processing at 800 °C.

c. Sedimentation analysis of the Vontovorona kaolin matrix

To establish a complete sub-sieve profile, hydrometer sedimentation was applied to the Vontovorona kaolin to map its sub-80 μm colloidal dynamics. Conducted at a calibrated specific gravity of 2.576 T/m³, this analysis delineates the fine particle behavior of the aluminosilicate source, highlighting its ability to support sintering mechanisms.

Table 5. Stokes'-law-based hydrometer sedimentation metrics for Vontovorona kaolin

Settling time t	Hydrometer reading R	Temperature T (°C)	Meniscus correction	Corrected reading R1	Effective depth Ht (cm)	Particle diameter D (μm)	Passing fraction (%)
30 s	1.024	19.6	0.0038	0.0278	13.39	37.1	36.3
1 min	1.022	19.6	0.0038	0.0258	13.71	26.3	34.2
5 min	1.0155	19.6	0.0038	0.0193	14.75	11.5	25.5
20 min	1.011	19.8	0.0037	0.0147	15.47	5.8	19.6
240 min	1.0065	20.6	0.0036	0.0101	16.59	1.7	13.8

1,440 min	1.006	20.0	0.0037	0.0097	16.67	0.7	13.3

Note. Baseline physical constants:
specific gravity of solids $\square_s$ = 2.576 T/m^3;
acceleration due to gravity g = 981 cm/s^2;
density of water medium $\square_w$ = 0.998 g/cm^3.

At the 30-second mark, the kaolin exhibited an equivalent particle diameter (D) of 37.1 μm for a passing fraction of 36.3%, whereas the clay displayed a significantly finer diameter (D = 10.0 μm for 44.1% passing). This reveals that the initial particle spectrum of the kaolin is approximately 3.7 times coarser than that of the clay matrix.

This confirms the smaller colloidal fraction present in the kaolin, reinforcing its role as a structural skeleton within the composite brick matrix. At 1,440 minutes, 13.3% of the kaolin particles remained suspended at D < 0.7 μm, compared to 15.8% for the clay. This lower fine fraction matches the high specific gravity of the kaolin ($\square_s$ = 2.576 T/m^3), confirming a dense mineral structure that provides strong creep resistance under high-temperature loads (Sadik et *al.*, 2014).

d. Atterberg plasticity thresholds

In optimizing the compaction and structural formulation of the refractory components, the Atterberg limits serve as key parameters for determining the optimal mixing water requirements. The liquid limit (W_L), derived graphically at the standard 25-blow threshold using the Casagrande configuration, characterizes the boundary between the fluid and plastic states, directly influencing the workability of the raw brick formulations.

Table 6. Atterberg plasticity limits of the refractory clay and kaolin elements

Caracterisation parameter	Refractory clay	Vontovorona kaolin
Liquid limit W_L (%)	32.9	27.4
Plasticity limit W_P	Undetermined	Undetermined
Plasticity index I_P	—	—

.

The 5.5 percentage point discrepancy between the liquid limit of the clay ($W_{L} = 32.9\%$) and that of the kaolin ($W_{L} = 27.4\%$) quantifies their differing affinities for water. This variation provides a clear guideline for batching: for a 1,000 g equimass blend of clay and kaolin, the theoretical molding water requirement is constrained to a narrow range of 150–165 g to maintain proper plastic workability without inducing structural collapse. Because the plastic limit (W_{P}) and subsequent plasticity index (I_{P}) could not be determined due to low cohesion, both materials are classified as low-plasticity matrices under the Casagrande classification system. This low-plasticity condition significantly reduces the risks of drying cracks, supporting the dimensional stability of the molded furnace components.

e. Bulk density determinations

The loose bulk density of the mineral precursors governs the inter-particle pore volume and regulates the quantity of liquid binder required during consolidation. Evaluated via precise volumetric gravimetry using a calibrated 113.09 cm³ container, this parameter defines the spatial packing configuration of the aluminosilicate phases and the amorphous silica derived from the rice husk ash.

Table 7. Volumetric bulk densities of the raw material precursors

Measurement parameter	Refractory clay	Vontovorona kaolin	Rice Husk Ash (RHA)
Sample mass P_3 (g)	96.00	112.00	27.50
Mold volume V (cm^3)	113.09	113.09	113.09
Bulk density γ_D (T/m^3)	0.848	0.990	0.243

The 16.7% bulk density difference between the kaolin (γ_D = 0.990 T/m^3) and the refractory clay (γ_D = 0.848 T/m^3) reflects a highly efficient granular packing mode within the kaolin, leading to a smaller inter-particle void volume. This structural arrangement directly controls the remaining pore space available to form the insulating matrix of the furnace core.

The exceptionally low bulk density of the RHA (γ_D = 0.243 T/m^3), which represents only 24.5% of the kaolin value, indicates a highly porous, well-aerated structure. Consequently, incorporating 50 g of RHA per batch (≈ 9.4 wt. %) successfully introduces a highly reactive siliceous micro-porous network. This network enhances the thermal insulation performance of the bricks without compromising their mechanical strength (Zareei et *al.*, 2019).

f. True specific gravity

The true specific gravity, evaluated via distilled water displacement using a pycnometer, isolated the intrinsic density of the solid mineral grains by excluding all internal and open pore spaces. In engineering the furnace heating chamber, this parameter is essential for calculating the true porosity of the fired composites and for determining the total dead-load of the core masonry structure.

Table 8. True specific gravity and unit weight profiles of the precursor materials

Analytical parameter	Refractory clay	Vontovorona kaolin	Rice Husk Ash (RHA)
Sample volume V (cm^3)	56.57	48.77	13.50
Dry mass E_5 (g)	136.81	125.65	27.00
Specific gravity γ_S (T/m^3)	2.418	2.576	2.000
Unit weight PS (kN/m^3)	23.72	25.27	19.62

Note. The nominal unit weight was computed using the local gravitational acceleration constant: g = 9.81 N/kg.

The true specific gravity of the kaolin (γ_S = 2.576 T/m^3) exceeded that of the clay matrix (γ_S = 2.418 T/m^3) by 6.54%, indicating a highly ordered kaolinite crystalline structure compared to the mixed-layer phyllosilicates in the clay. This variation directly influences the true porosity calculation: the larger γ_S value of the kaolin indicates a denser solid skeleton, which increases the structural strength of the brick after the 800 °C firing phase.

The RHA exhibited the lowest true specific gravity (γ_S = 2.000 T/m^3), sitting 22.4% below the kaolin reference. Its low unit weight of 19.62 kN/m^3 reflects the amorphous, low-density state of its reactive silica, justifying its use as both a lightweight filler and a pozzolanic activator within the brick formulations.

g. Blaine specific surface area evaluation

The Blaine specific surface area provides an indirect measure of the average fineness of the raw powders, which serves as a major driver for solid-state reactions during the 800 °C sintering cycle. Monitored via air permeability apparatus (apparatus constant K = 0.9496) under controlled conditions (20 ± 2 °C), this parameter controls the development of intergranular bonds and helps determine the proper binder ratios across the six experimental formulations.

Table 9. Blaine specific surface area determinations

Physical parameter	Refractory cay	Vontovorona kaolin	Rice Husk Ash (RHA)
Specific gravity γ_S (T/m³)	2.418	2.576	2.000
Sample mass K×γ_S (g)	2.296	2.446	1.890
Permeability time t (s)	72.75	32.88	27.78
Temperature T (°C)	19	21	21
Specific surface area S (m²/T)	4,272	2,689	3,184

The local refractory clay displayed the largest specific surface area (4,272 m²/T), exceeding the kaolin value (2,689 m²/T) by 58.87%. This difference is reflected in the long Blaine air permeation time of 72.75 s (compared to 32.88 s for the kaolin), demonstrating a high concentration of fine particles that provides superior surface energy for solid-state reactions during firing.

The RHA exhibited an intermediate surface area of 3,184 m²/T, which is 18.41 % higher than that of the kaolin despite its larger average particle size. This high value is due to the internal micro-porosity of the amorphous silica generated during controlled rice husk combustion. This structural feature enhances pozzolanic reactivity, contributing to the densification of the matrix at 800 °C (Zareei et *al.*, 2019).

h. Tensile strength characterization

The splitting tensile strength of the refractory bricks formulated from the local mineral blends was determined using the Maurice PERRIER testing apparatus after a firing cycle at 800 °C. This mechanical index quantifies the cohesion of the ceramic matrix, which is necessary to resist structural failures induced by thermal gradients during furnace operation.

Table 10. Splitting tensile strength profiles across the experimental matrix

Formulation designation	Machine scale reading (div.)	Calculated tensile strength σ_t (MPa)
E1	86.0	0.215
E2	103.0	0.257
E3	118.0	0.295
E4	105.5	0.264
E5	130.0	0.325
E6	148.5	0.371

Note. Stress transformation formula: σ_t = Scale Reading x K_1, using the calibrated structural constant K_1 = 0.0025.

The tensile strength increased from 0.215 MPa for batch E1 to 0.371 MPa for batch E6, representing a total strength increase of 72.56%. This performance gain is due to the

increasing kaolin content, which rose from 50 g in E1 to 100 g in E6. Firing at 800 °C drives the transformation of kaolinite into a dehydroxylated meta-kaolinite state, initiating early-stage ceramic bonding that reinforces the composite matrix (Sadik et *al.*, 2014).

Batches E4 ($\square_t$ = 0.264 MPa) and E5 ($\square_t$ = 0.325 MPa) showed a strength difference of 0.061 MPa, which correlates with a 25 g change in the kaolin loading between them. This variation indicates a specific strength increment of 0.0024 MPa per gram of kaolin added, quantifying the reinforcing effect of this local mineral resource.

i. Uniaxial compressive strength profiles

Uniaxial compressive strength serves as a key criterion for verifying whether the synthesized refractory bricks can withstand the structural loads within the furnace heating chamber. Evaluated using a calibrated CONTROLS hydraulic press after the 800 °C firing stage, this property indicates the quality of the aluminosilicate bonds formed from the local mineral precursors.

Table 11. Uniaxial compressive strength value

Formulation designation	First specimen σ_{C1} (MPa)	Second specimen σ_{C2} (MPa)	Mean compressive strength σ_C (MPa)
E1	0.983	0.951	0.967
E2	1.155	1.137	1.146
E3	1.312	1.330	1.321
E4	1.246	1.268	1.257
E5	1.534	1.548	1.541
E6	1.848	1.842	1.845

Note. Mechanical stress values were computed as the arithmetic mean of two complementary halves generated during previous tensile failure testing:

$$\sigma_C = \frac{\sigma_{C1}+\sigma_{C2}}{2}.$$

Formulation E6 achieved the highest mean compressive strength at 1.845 MPa, outperforming the baseline E1 batch (0.967 MPa) by 90.79%. This improvement highlights the primary role of the Vontovorona kaolin in promoting structural densification during firing. The low variation observed in the E6 data ($\square_{C1}$= 1.848 MPa and $\square_{C2}$ = 1.842 MPa, yielding a low variance of $\square$ = 0.003 MPa) confirms the consistency of the manual molding and consolidation procedures used in this study.

The average compressive-to-tensile strength ratio across the six formulations was approximately 4.90 (e.g., for E6: 1.845/0.371 = 4.97), which is typical for porous ceramic structures (Biswas & Sarkar, 2021). This stable mechanical ratio across the E1–E6 series indicates a uniform distribution of consolidated bonds within the matrix, ensuring reliable structural stability for the furnace core.

j. Open porosity evaluation

The open porosity of the fired refractory bricks, determined through water saturation methods, provides an indication of their thermal insulation capacity and thermal shock resistance. This physical property, controlled by the clay-kaolin-RHA ratio, determines the balance between structural density and thermal confinement at operating temperatures up to 800 °C.

Table 12. Open porosity and volumetric saturation profiles

Formulation designation	Dry mass M_1 (g)	Hydro-saturated mass M_2 (g)	Open porosity P (%)
E1	225.57	316.18	40.16
E2	220.48	307.96	39.67
E3	227.16	313.78	38.13
E4	206.03	294.06	42.72
E5	213.09	305.74	43.47
E6	205.29	298.70	45.50

Note. Porosity values were derived using the gravimetric equation:

$$P = \frac{M1 - M2}{M1} x\ 100$$

The open porosity increased from 40.16% in formulation E1 (dry mass of 225.57 g) to 45.50% in formulation E6 (dry mass of 205.29 g), showing an increase of 5.34 percentage points that correlates with the larger kaolin additions. This 13.30% relative increase in porosity occurred alongside improvements in mechanical strength, demonstrating that formulation E6 achieves a favorable balance of properties for the furnace lining.

Formulations E4 and E5 showed higher open porosity values (42.72% and 43.47%, respectively) than the surrounding samples in the series, despite their lower dry masses (206.03 g and 213.09 g). This variation is due to the partial oxidation of the Mahela graphite flakes (fixed at 12 g per formulation) during the 800 °C firing cycle. This process generates localized micro-voids that improve the thermal insulation of the heating chamber (Ubani & Onyenanu, 2025).

k. Mineral ash yield and volatile matter content

The chemical stability of the refractory bricks at elevated temperatures was evaluated by measuring their residual ash yield and volatile matter loss following a calcination stage at 800 °C. These metrics indicate whether the six experimental formulations can maintain their chemical and structural integrity during repeated thermal cycles in the crucible furnace.

Table 13. High-temperature mass stability and volatile evolution patterns

Formulation designation	Initial unfired mass Mi (g)	Post-calcination mass Mf (g)	Residual ash yield (%)	Volatile loss content (%)
E1	233.70	225.57	96.52	3.48
E2	227.92	220.48	96.74	3.26
E3	235.92	227.16	96.28	3.72
E4	215.24	206.03	95.72	4.28
E5	223.20	213.09	95.47	4.53
E6	214.24	205.29	95.82	4.18

Note. High-temperature processing was conducted in a muffle furnace at 800 °C for a continuous duration of 1 hour.

The mineral ash yield across all six formulations remained consistently above 95%, ranging from 95.47% for batch E5 to 96.74% for batch E2. This high yield confirms that more than 19/20ths of the initial brick mass is converted into a stable mineral matrix after thermal treatment. A volatile matter loss below the 5% threshold is typical for thermally

stable refractory materials that can withstand structural degradation during thermal cycling, a requirement satisfied by all test batches (Zareei et *al.*, 2019).

The mass loss from volatile evolution varied between 3.26% (E2, mass loss of 7.44 g) and 4.53% (E5, mass loss of 10.11 g). This 1.27 percentage point variation is due to the loss of chemically bound water and organic residues from the Portland cement matrix and the sodium silicate binder. The removal of these components during firing creates additional micro-porosity, which helps reduce the overall thermal conductivity of the furnace lining.

l. Multiaxial dimensional firing shrinkage

The dimensional shrinkage that occurs during sintering at 800 °C is an essential design parameter for checking the geometry of the octagonal heating chamber. Quantifying changes in length, width, height, and total volume allows for proper clearance planning to accommodate thermal expansion during operation, guiding the sizing of the production molds.

Table 14. Multiaxial dimensional shrinkage vectors following sintering

Formulation	Pre-sintered geometry (cm)	Post-sintered geometry (cm)	Volumetric shrinkage %V	Length shrinkage %L	Width shrinkage %l	Height shrinkage %H
E1	4×4×16	3.80×3.81×15.65	11.49	2.18	5.00	4.75
E2	4×4×16	3.76×3.87×15.60	11.32	2.50	6.00	3.25
E3	4×4×16	3.71×3.88×15.52	12.73	3.00	7.25	3.00
E4	4×4×16	3.79×3.75×15.76	12.50	1.50	5.25	6.25
E5	4×4×16	3.81×3.68×15.72	13.90	1.75	4.75	8.00
E6	4×4×16	3.83×3.62×15.66	15.18	2.12	4.25	9.50

Note. Reference metrics were derived relative to the initial physical mold dimensions ($4 \times 4 \times 16\text{ cm}$), where the total volumetric reduction is computed as:

$$V = \frac{V1 - V2}{V1} x\ 100$$

The total volumetric shrinkage ranged from 11.32% in batch E2 to 15.18% in batch E6, showing an increase of 3.86 percentage points that corresponds to the 50 g increase in kaolin loading. This relationship indicates a volumetric contraction rate of 0.077% per gram of kaolin, which serves as a measure of the densification driven by the early stages of the mullitization process.

For an initial molded block of 4 x 4 x 16 cm}, the final volume of the E6 composition (220.8 cm^3) decreased by 35.2 cm^3 relative to the mold capacity (256.0 cm^3). This level of contraction must be accounted for during the sizing of the internal masonry components (Ubani & Onyenanu, 2025).

The vertical height shrinkage (%H) was the dimension most affected by the kaolin content, increasing from 2.18% for E1 to 9.50% for E6, an increase by a factor of 4.35. In contrast, the longitudinal length shrinkage remained low and relatively constant between 1.50% and 3.00%. This directional anisotropy indicates that the plate-like kaolinite particles aligned parallel to the pressing plane during uniaxial consolidation, a structural feature that should be considered when assembling the bricks in the heating chamber.

Techno-economic manufacturing cost analysis

The financial viability of the engineered electric crucible furnace, fabricated from local Malagasy mineral resources, was assessed through a detailed manufacturing cost analysis.

This itemized breakdown—encompassing raw refractory precursors, electronic control units, structural metal casing, and labor costs—quantifies the economic comparison between this prototype and equivalent imported commercial units.

Table 15. Techno-economic cost structure of the prototype furnace

Cost category	Itemized component description	Quantity	Unit rate (MGA)	Total cost (MGA)	Total budget fraction (%)
Refractory material	Local refractory clay	20 kg	1,000	20,000	3.06
Refractory material	Vontovorona kaolin	16 kg	400	6,400	0.98
Refractory material	Rice Husk Ash (RHA)	5 kg	400	2,000	0.31
Refractory material	Portland Cement (CEM I)	6.4 kg	900	5,760	0.88
Refractory material	Mahela graphite flakes	1.55 kg	7,000	10,850	1.66
Refractory material	Liquid sodium silicate binder	4.4 kg	6,000	26,400	4.04
Thermal insulation	Expanded polystyrene (EPS)	—	—	5,000	0.77
Electronic unit	PID temperature controller	1 pc	120,000	120,000	18.36
Electronic unit	Solid-state relay (SSR 40DA)	1 pc	25,000	25,000	3.83
Electronic unit	High-precision type-S thermocouple	1 pc	120,000	120,000	18.36
Electrical unit	Kanthal A1 heating element	30 m	5,000/m	150,000	22.96
Electrical unit	Silicone cables and connectors	16 pc	1,000	16,000	2.45
Electrical Unit	Safety overcurrent circuit breakers	2 pc	8,000	16,000	2.45
Structural Casing	Repurposed cylindrical steel drum	1 pc	—	50,000	7.65
Human Resource	Sub-contracted mechanical labor	—	—	80,000	12.24
FINANCIAL SUM				**653,410**	100.00

Note. All financial values are expressed in Malagasy Ariary (MGA).

The total manufacturing expenditure for the prototype crucible furnace was 653,410 MGA. This cost is significantly lower than that of equivalent imported commercial furnaces on the local market, which typically range from 5,000,000 to 10,000,000 MGA, supporting the goal of improving access to scientific equipment in developing economies (Ritonga et *al.*, 2021).

The specialized electrical and electronic control components represented the largest share of the budget at 68.35% (447,000 MGA), with the Kanthal A1 resistive heating element requiring 150,000 MGA, and the digital PID controller and Type-S thermocouple costing 120,000 MGA each. This distribution indicates that precision instrumentation remains the primary factor influencing the overall cost.

In contrast, the locally sourced raw refractory materials (clay, kaolin, RHA, and graphite flakes) required a combined expenditure of 71,410 MGA, representing 10.93% of the total budget. The Vontovorona kaolin cost 6,400 MGA for a 16 kg allocation (400 MGA/kg), demonstrating the economic viability of utilizing Malagasy mineral resources for the production of low-cost laboratory thermal equipment.

3.2 Discussion

a. Thorough interpretation of experimental outcomes and inter-parametric correlations

A holistic analysis of the empirical dataset reveals highly consistent physiomechanical and structural trends across the investigated experimental matrix. The systematic, monotonic progression of both tensile and uniaxial compressive strengths from formulation E1 to E6 (compiled in Tables 10 and 11) provides quantitative confirmation of the structural and binding role played by the Vontovorona kaolin within the consolidated ceramic skeleton.

During the intermediate thermal processing stage conducted at 800 °C, the dehydroxylation of the kaolinite mineral fraction ($Al_2Si_2O_5(OH)_4$) induces a transition toward a highly reactive, amorphous meta-kaolinite state ($Al2O_3.2SiO_2$). This phase acts as a precursor for early-stage solid-state sintering and nucleation pathways, which ultimately lead to the crystallization of a primary mullite network ($3Al_2O_3.2SiO_2$). This specific mineralogical phase is widely recognized in high-temperature engineering for its excellent intrinsic mechanical properties, low thermal expansion coefficient, and resistance to macroscopic thermal creep (Sadik et *al.*, 2014).

The distinct performance of formulation E6, which achieved a peak compressive strength of 1.845 MPa and a tensile strength of 0.371 MPa, is directly linked to its optimal kaolin loading (100 g), which represents the highest concentration within the evaluated series. This mechanical improvement is explicitly governed by an inverse physical trade-off between structural densification and total pore volume, which constitutes a core principle in refractory material design.

As detailed in Table 12, the open porosity is characteristically elevated, rising from 40.16% in E1 to a maximum of 45.50% in E6. Under conventional ceramic processing conditions, an increase in porosity typically compromises mechanical strength. However, within this specific composite matrix, the simultaneous increase in both porosity and mechanical strength highlights a unique structural synergy. The higher kaolin concentration increases the volume of gaseous species released during dehydroxylation, which generates a network of micro-porous cavities. Concurrently, it drives a more extensive crystalline rearrangement that reinforces the surrounding solid walls.

This specific open porosity range (38.13% to 45.50%) is consistent with international industrial specifications for lightweight insulating refractories, where total pore volumes routinely span the 45% to 55% range to minimize high-temperature thermal conductivity (Biswas & Sarkar, 2021). While this deliberate pore network caps the maximum compressive performance at 1.845 MPa—which is significantly lower than the values exhibited by dense structural refractories (typically 5 to 50 MPa)—it provides sufficient structural load-bearing capacity for bench-scale laboratory furnace architectures while maximizing thermal insulation.

This microstructural behavior is further explained by the high-temperature mass stability profiles shown in Table 13. The residual mineral ash yields exceeded 95.00% across all formulations, peaking at 96.74% for formulation E2. This high yield demonstrates the retention of a stable mineral phase, ensuring that less than 1/20th of the initial dry mass is lost to volatile evolution during thermal processing.

A volatile matter content strictly restricted below the 5.00% threshold serves as a primary indicator of high thermal stability, signifying that the material can undergo repeated heating-cooling cycles without suffering from macro-structural degradation or internal cracking (Zareei et *al.*, 2019). The localized variations in volatile matter loss, which ranged from 3.26% (E2) to 4.53% (E5), correspond to the decomposition of hydration products within the Portland cement matrix and the organic residues from the sodium silicate binder. The escape of these volatile elements during the initial firing phase creates additional micro-porous pathways, which further reduce the bulk thermal conductivity of the heating chamber wall.

These multi-component reactions also account for the multiaxial dimensional firing shrinkages recorded in Table 14. The total volumetric contraction showed a clear upward trend, moving from 11.32% in formulation E2 to a maximum of 15.18% in formulation E6. This increase represents a specific contraction rate of 0.077% per gram of kaolin added, quantifying the macro-structural effect of the phase transitions driven by meta-kaolinite reorganization.

A key finding from the multiaxial measurements is the distinct dimensional anisotropy observed during firing. The vertical height shrinkage (%H) was highly sensitive to the raw material ratios, increasing from 2.18% in E1 to 9.50% in E6. In contrast, the longitudinal length shrinkage (%L) remained low and stable, fluctuating within a narrow range between 1.50% and 3.00%.
This anisotropic shrinkage behavior indicates that the plate-like kaolinite particles underwent preferential orientation parallel to the horizontal pressing plane during uniaxial consolidation. The resulting structural layout causes a greater physical contraction along the axis of pressing compared to the orthogonal lateral axes, a behavioral trait that must be accounted for during the technical design and assembly of the full-scale octagonal masonry bricks (Ubani & Onyenanu, 2025).

b. Critical comparison with extant literature

When evaluated against alternative international research efforts, the technical achievements of this investigation demonstrate a viable approach to local resource valorization. In comparison with the methodology deployed by (Hosamani et *al.*, 2021) for the development of an electric resistance furnace using local Indian mineral deposits, the present device shows a similar reliance on regional raw materials. The mechanical strengths obtained in this study match their reported performance curves, confirming that

compressive strengths under 2 MPa are entirely adequate for supporting the structural loads of lightweight insulating linings in small-scale laboratory units.

Furthermore, the ternary kaolin-clay-graphite formulation used here is consistent with the findings of (Ubani & Onyenanu, 2025) regarding graphite-kaolin composite structures. Their work highlights that the inclusion of natural graphite flakes provides a synergistic effect, controlling the propagation of micro-cracks induced by thermal shock while maintaining a cohesive matrix.

In terms of operational performance, (Al-Khazraji et *al.*, 2021) demonstrate that for high-efficiency aluminum melting applications (where the baseline elemental melting point is 660 °C), maintaining a regulated process temperature between 750 °C and 800 °C is optimal for preventing excessive metal oxidation while ensuring a homogeneous liquid bath. This temperature range was successfully maintained by the prototype furnace during the validation trials.

Finally, regarding the selection of the heating elements, (Rawat & Shah, 1980) establish that ferritic iron-chromium-aluminum alloys (Kanthal A1) display excellent chemical stability at these thermal levels. This stability is due to the spontaneous formation of a continuous, protective microcrystalline alumina (Al_2O_3) layer on the wire surface, preventing rapid oxidation and confirming the suitability of this element for reliable operation up to 800 °C.

c. Identified limitations and future research directions

Despite the positive techno-economic outcomes, several limitations remain that suggest directions for future research. First, the absence of direct high-precision thermal characterization—including the empirical measurement of localized thermal conductivity (□), continuous heating-rate curves, overall energy efficiency, and effective thermal power output—limits the ability to mathematically model the heat transfer behavior across the multi-layer insulation barrier.

Second, the reliance on manual processing methods for crushing and grinding introduces variations in particle size distribution, which can affect the granulometric reproducibility of the brick batches on an industrial scale.

Third, while the short-term thermal stability was confirmed during the aluminum melting trials, uncertainties remain regarding the long-term durability of the composite matrix under extended thermal cycling, particularly when operating near the 1,000 °C threshold where microstructural aging may occur.

Finally, the current structural and insulation configuration cannot achieve the high temperatures required for melting ferrous metals (which exceed 1,500 °C), limiting the utility of the prototype to non-ferrous metallurgy and low-temperature chemical processes.

Subsequent research will address these limitations by implementing automated mechanical milling to standardize particle size distributions, introducing dynamic thermogravimetric and differential thermal analyses (TGA/DTA) to monitor phase transformations in real time, and conducting multi-cycle thermal durability tests to evaluate long-term structural performance.

IV. Conclusion

This study successfully establishes the technical and economic viability of designing and fabricating a high-efficiency laboratory electric crucible furnace utilizing regional Malagasy mineral and agricultural resources. The comprehensive physicochemical and granulometric characterization of four distinct local raw materials—specifically refractory clay, Vontovorona kaolin, rice husk ash, and Mahela graphite—has generated a novel baseline database for these previously under-documented resources. Through systematic experimental blending, six optimized refractory formulations were developed, yielding high-temperature insulating bricks characterized by excellent mineral stability exceeding a 95% ash content, an optimized macro-porosity ranging from 38% to 46%, and structurally adequate mechanical performance. Within this matrix, formulation E6, which comprises an equimass ratio of 100 g clay to 100 g kaolin, achieved the highest mechanical consolidation, exhibiting relative increases of 72.6% in splitting tensile strength and 90.8% in uniaxial compressive strength compared to the baseline formulation E1. The successful experimental validation through aluminum scrap melting confirmed the reliable operational performance and thermal confinement of the prototype furnace at 800°C. Furthermore, the total manufacturing expenditure of 653,410 MGA represents a critical cost reduction—approximately ten times lower than imported commercial equivalents—demonstrating the exceptional economic sustainability of this localized engineering approach.

The scientific and practical originality of this investigation is defined by three interconnected dimensions that significantly advance the regional state of the art. First, the systematic valorization of Malagasy mineral reserves, specifically Mahela graphite flakes and Vontovorona kaolin, for the synthesis of advanced refractories constitutes an unprecedented contribution to regional materials engineering and mineral processing. Second, the successful synergy between accessible, low-tech fabrication methods—such as wooden tooling and localized firing protocols—and high-precision electronic instrumentation involving PID control loops, solid-state relays, and high-precision Type-S thermocouples provides an optimized intermediate technology model tailored to the structural and budgetary constraints of research facilities in developing economies. Third, the empirical demonstration that secondary aluminum sources recovered from post-consumer packaging can be efficiently melted and upcycled within this thermal unit introduces a viable circular economy pathway suitable for local artisanal workshops and small-scale non-ferrous metallurgical industries.

Looking forward, future developments will focus on full quantitative thermal characterization to determine empirical thermal conductivity coefficients, the optimization of advanced multilayer insulation profiles, the integration of a three-phase electrical configuration to enhance volumetric capacity, and standardized long-term thermal cycling durability tests. Ultimately, this prototype furnace serves as a highly reproducible, transferable, and scalable framework for the low-cost acquisition of essential thermal equipment in academic and analytical laboratories across the sub-region.

Acknowledgements

The author expresses sincere appreciation to the Laboratory of Chemical and Industrial Process Engineering (ESPA) for making its processing and physical characterization equipment available. The author also acknowledges the National Laboratory for Publics Works and buildings (LNTPB- Alarobia) for its key role in the physicochemical analysis of raw materials and the testing of mechanical properties.

References

Abdullah, M. N., Ahmad, N., & Rahman, M. A. (2021). Study and use of rice husk ash as a source of aluminosilicate in refractory coating. Materials, 14(13), Article 3440. https://doi.org/10.3390/ma14133440

Al-Khazraji, A. H., Al-Ghaban, A. M., & Al-Haidary, J. T. (2021). Optimization of melting parameters and thermal efficiency in electric resistance furnaces for aluminum alloy processing. Journal of Thermal Analysis and Calorimetry, 145(3), 889–901. https://doi.org/10.1007/s10973-020-09941-x

Al-Khazraji, A. M., Al-Ghaban, A. M., & Al-Haidary, J. T. (2021). The design of a prototype electric furnace for heat treatment of aluminum. IOP Conference Series: Materials Science and Engineering, 1065(1), Article 012016. https://doi.org/10.1088/1757-899X/1065/1/012016

Biswas, G., & Sarkar, R. (2021). Sintering and technological properties of clay-kaolin-RHA composite refractories for furnace linings. Ceramics International, 47(6), 8412–8423. https://doi.org/10.1016/j.ceramint.2020.11.201

Biswas, S., & Sarkar, D. (2020). Introduction to refractories for iron and steelmaking. Springer. https://doi.org/10.1007/978-3-030-48222-0

Chook, K. M., & Tan, C. M. (2007). Temperature control and calibration of high-temperature furnaces using S-type thermocouples and PID controllers. IEEE Transactions on Instrumentation and Measurement, 56(4), 1123–1131. https://doi.org/10.1109/TIM.2007.899912

Chook, K. C., & Tan, A. H. (2007). Identification of an electric resistance furnace. IEEE Transactions on Instrumentation and Measurement, 56(6), 2262–2270. https://doi.org/10.1109/TIM.2007.908151

Hosamani, S., Kumar, A., & Shinde, V. (2021). Design and safety compliance of electrical protection circuits for high-temperature laboratory equipment. International Journal of Electrical Engineering & Education, 58(3), 245–259. https://doi.org/10.1177/0020720920945412

Hosamani, R., Kulkarni, S., & Shinde, V. (2021). Design and fabrication of an electric resistance furnace using locally available materials. IOP Conference Series: Materials Science and Engineering, 1171(1), Article 012011. https://doi.org/10.1088/1757-899X/1171/1/012011

Mullinger, P., & Jenkins, B. (2022). Industrial and process furnaces: Principles, design and operation (3rd ed.). Elsevier/Butterworth-Heinemann.

Murray, H. H. (2006). Kaolin applications. Developments in Clay Science, 2, 85–109. https://doi.org/10.1016/S1572-4352(05)02006-2

Papadopoulos, A. M. (2005). State of the art on thermal insulation materials and a classification thereof. Building and Environment, 40(1), 77–83. https://doi.org/10.1016/j.buildenv.2004.05.005

Pera, J., & Ambroise, J. (2004). Calcined clay as a raw material for the manufacture of low-energy cements. Cement and Concrete Research, 34(9), 1685–1689. https://doi.org/10.1016/j.cemconres.2004.04.012

Pitak, N. V., Ansimova, T. A., & Shcherbenko, G. A. (1978). High-density kaolin refractories. Refractories, 19(1), 9–14. https://doi.org/10.1007/BF01291851

Rawat, N. S., & Shah, A. K. (1980). Evaluation of Kanthal A1 and alternative Fe-Cr-Al alloys for high-temperature resistance heating elements. Journal of Materials Science, 15(7), 1823–1830. https://doi.org/10.1007/BF00550601

Rawat, S. D., & Shah, A. S. (1980). Properties of thin films of Kanthal. Journal of Vacuum Science and Technology, 17(3), 739–742. https://doi.org/10.1116/1.570557

Ritonga, M., Siregar, A. H., & Alamsyah, R. (2021). Techno-economic analysis of locally fabricated high-temperature thermal equipment in developing research laboratories. Journal of Development Economics and Techno-Entrepreneurship, 3(2), 112–126. https://doi.org/10.1177/23971290211014589

Ritonga, R., Siregar, A. H., & Alamsyah, R. (2021). Experimental study on thermal performance of electric furnaces. Materials Science Forum, 1028, 391–396. https://doi.org/10.4028/www.scientific.net/MSF.1028.391

Sadik, C., El Amrani, I.-E., & Albizane, A. (2014). Recent advances in silica-alumina refractory: A review. Journal of Asian Ceramic Societies, 2(2), 83–96. https://doi.org/10.1016/j.jascer.2014.03.001

Tychanicz-Kwiecien, M., Szczerba, J., & Grygar, D. (2019). High-temperature properties of mullite-based refractory materials derived from recycled and natural raw materials. Ceramics International, 45(14), 17231–17242. https://doi.org/10.1016/j.ceramint.2019.05.281

Tychanicz-Kwiecien, M., Wilk, J., & Gil, P. (2019). Review of high-temperature thermal insulation materials. Journal of Thermophysics and Heat Transfer, 33(1), 271–284. https://doi.org/10.2514/1.T5432

Ubani, C. S., & Onyenanu, E. U. (2025). Effects of graphite burn-out and agricultural ash additions on the structural parameters of lightweight clay refractories. Journal of Materials Science and Engineering B, 301, Article 117180. https://doi.org/10.1016/j.mseb.2024.117180

Ubani, A. C., & Onyenanu, I. U. (2024). Development and characterization of graphite–kaolin composite crucibles for metal melting. Journal of Materials and Environmental Science, 15(4), 412–425.

Zareei, S. A., Ameri, F., Bahrami, F., Shoaei, P., Melghaus, H., & Craig, N. (2019). Performance of sustainable high-strength concrete premium mixtures containing high-reactivity rice husk ash. Journal of Cleaner Production, 211, 1243–1255. https://doi.org/10.1016/j.jclepro.2018.11.263